



LAWRENCE
LIVERMORE
NATIONAL
LABORATORY

Comparison of two- and three-dimensional simulations of miscible Rayleigh-Taylor instability

W. Cabot

February 27, 2006

Physics of Fluids

Disclaimer

This document was prepared as an account of work sponsored by an agency of the United States Government. Neither the United States Government nor the University of California nor any of their employees, makes any warranty, express or implied, or assumes any legal liability or responsibility for the accuracy, completeness, or usefulness of any information, apparatus, product, or process disclosed, or represents that its use would not infringe privately owned rights. Reference herein to any specific commercial product, process, or service by trade name, trademark, manufacturer, or otherwise, does not necessarily constitute or imply its endorsement, recommendation, or favoring by the United States Government or the University of California. The views and opinions of authors expressed herein do not necessarily state or reflect those of the United States Government or the University of California, and shall not be used for advertising or product endorsement purposes.

Comparison of two- and three-dimensional simulations of miscible Rayleigh-Taylor instability

W. Cabot

University of California,

Lawrence Livermore National Laboratory,

*Livermore, CA 94550**

Abstract

A comparison of two-dimensional and three-dimensional high-resolution numerical large-eddy simulations of planar, miscible Rayleigh-Taylor instability flows are presented. The resolution of the three-dimensional simulation is sufficient to attain a fully turbulent state. A number of different statistics from the mixing region (e.g., growth rates, PDFs, mixedness measures, and spectra) are used to demonstrate that two-dimensional flow simulations differ substantially from the three-dimensional one. It is found that the two-dimensional flow grows more quickly than its three-dimensional counterpart at late times, develops larger structures, and is much less well mixed. These findings are consistent with the concept of inverse cascade in two-dimensional flow, as well as the influence of a reduced effective Atwood number on miscible flow.

*Electronic address: cabot1@llnl.gov

I. INTRODUCTION

Two-dimensional numerical simulations can provide an economical means for exploring flow behavior. However, they are only strictly valid when applied to flows that are inherently two-dimensional, or nearly so, such that variations in the third dimension remain small on time scales of interest (e.g., [1]). Two- and three-dimensional flows develop quite differently [2], so the extent to which two-dimensional simulations can be used to represent three-dimensional turbulent flow is questionable [3]. Here this issue is examined specifically for Rayleigh-Taylor instability (RTI) flow, which develops when a heavy fluid is accelerated toward an adjoining light fluid with a perturbed interface. For this type of flow, the key statistics of interest are typically the rate of growth of the mixing region and the level of mixing therein.

In previous numerical simulations of RTI flow, it has generally been found for single-mode or long-wavelength initial perturbations of the heavy-light interface that the mixing layer grows more rapidly for 3D perturbations than for similar 2D perturbations [4, 5]. The results have been somewhat more equivocal in RTI flow simulations with initial interfacial perturbations comprising a broad range of scales. For direct numerical simulations (DNS) with pseudospectral methods performed by Young et al. [6], the flow started with random-phase, broadband initial perturbations at the interface and developed to a weakly turbulent state. The 2D simulations, initialized with planes of data from the 3D simulation, showed growth rates about half that of the 3D case. The ratio of kinetic energy to released potential energy in the 2D case was found to be about twice that of the 3D case. Weber et al. [7] performed 3D and 2D ALE simulations with the broadband initial conditions specified by the “ α -group” [8]; they also used planes of initial 3D data to initialize the 2D runs and found comparable rates of growth of the mixing region, despite markedly different flow structures. Youngs [9, 10] found in MILES simulations that the mixing region grew more rapidly at early times for the 3D case than the 2D case, but that the growth rates were comparable or even higher for the 2D case at late times as the 3D flow became turbulent. That 2D flow was initialized with a broadband spectrum analogous to that used in the 3D flow but lower in dimension. Youngs found that the 2D level of mixing was considerably lower than the 3D level, and that the 2D kinetic to potential energy ratio was twice that of the 3D ratio.

The single-mode RTI model developed by Goncharov [11] shows 3D perturbations growing at a rate $\sqrt{3}$ times faster than 2D perturbations. Bubble-merger models [12, 13] have been constructed that give comparable rates of mixing layer growth for 2D and 3D perturbations. While the 3D single-mode bubble growth is faster in these models, different geometrical effects of the merging process between 3D and 2D offset this advantage in multimode development.

Recently, very large 3D large-eddy simulations of planar, miscible RTI flow were performed with broadband initial perturbations [14], in which the flow becomes fully turbulent at late times. The statistics from these 3D RTI simulations are compared here with similar 2D simulations in a flow regime not previously attainable. The simulations are described briefly in §II; statistics from 2D and 3D simulations are compared in §III; and conclusions are presented in §IV.

II. CALCULATIONS

A. 3D Simulations

A large three-dimensional (3D) large-eddy simulation (LES) of planar, miscible, incompressible Rayleigh-Taylor instability (RTI) was performed by Cook et al. [14] using a 10th-order compact finite-difference scheme [15] for spatial derivatives and a third-order pressure-projection time advancement scheme. Artificial dissipation and diffusion models, as well as filtering with an 8th-order compact low-pass filter, were applied to stabilize the high-frequency components of the flow and to control unphysical density excursions; there was no explicit molecular viscosity or diffusivity used in the calculation. The effective model Schmidt number (mass diffusion coefficient divided by viscosity coefficient) was observed to be about 10 in the interior of the developed mixing region and closer to unity near the pure fluid fronts. The fluid is assumed to be molecularly mixed below grid resolution at points with intermediate fluid density. The governing equations and numerical techniques are described in detail in [14].

The 3D RTI flow had a density ratio of 3:1. The initial flow had a slightly diffuse interface between high and low density regions whose vertical position was seeded with two-dimensional horizontal perturbations. The perturbations were computed from a two-

dimensional horizontal spectrum with narrow gaussian band of high-frequency modes with random phases. The simulation was performed on a 1152^3 uniform cartesian grid. It was halted when the largest horizontal structures began to become poorly resolved, i.e., large scales had developed in the horizontal direction comparable to the size of the numerical domain, so that the flow was no longer independent of horizontal boundary conditions; there is also a concomitant reduction of statistical sample of large-scale flow features when this happens. At late times the flow was fully turbulent and had moved beyond the mixing transition [16].

B. 2D Simulations

The two-dimensional (2D) simulations used the same code, the same physical parameters, and the same grid resolution as the 3D simulation, but only one horizontal direction was computed on a 1152^2 grid. The practical result of this in the governing equations is that the velocity component and all spatial derivatives in the neglected direction vanish. Two different types of initial 2D perturbations were chosen corresponding to those used in previous numerical studies: (1) In case “2Db”, initial perturbations are computed from a one-dimensional horizontal spectrum with a gaussian *bump* at high frequencies. These perturbations have the same spectral shape and amplitude used in the two-dimensional perturbations for the 3D simulation, but with a different set of random phases. (2) In case “2Ds”, initial planes of density are extracted from *slices* of the initial density field for the 3D simulation. For different runs, different, widely spaced slices are chosen from both horizontal directions to preserve statistical independence. Sixteen 2D runs were performed for each initial perturbation spectrum to increase the statistical sample, although the work by Clark [17] suggests that a much larger ensemble may be required to guarantee converged statistics. The initial horizontal density spectral functions are shown in Fig. 1. The initial spectra for the 2Db simulations coincide exactly with the initial spectrum from the 3D simulation by design. Note that the initial spectra for the 2Ds simulations contain energy at long wavelengths; these initial conditions, which are planes of the initial 3D data, contain non-modal wavenumber contributions from the horizontal direction normal to the transformed direction, which “alias” [18] to all wavenumbers.

C. Physical Units

All LES runs have nearly the same initial horizontal integral length for the density perturbations, defined by

$$\lambda_0 = \int_0^\infty k^{-1} E_\rho(k) dk / \int_0^\infty E_\rho(k) dk , \quad (1)$$

where E_ρ is the horizontal spectral function for density at the initial interface between heavy and light fluids, and k is the wavenumber. It will be assumed throughout this paper that the unit of length is λ_0 , the unit of time is $\sqrt{\lambda_0/gA}$, and the unit of density is the density of the light fluid ρ_1 . The Atwood number, $A \equiv (\rho_2 - \rho_1)/(\rho_2 + \rho_1) = 1/2$, is a measure of the density contrast between the light fluid ρ_1 and the heavy fluid ρ_2 , and g is the magnitude of the gravity.

III. RESULTS

A. Structure

The difference in structure between 2D and 3D RTI flow at $t = 25$ is clearly seen in Fig. 2. At this stage the 3D mixing region is fully turbulent and exhibits fine-scale structure and large patches of mixed fluid, which appear light grey in the image [14, 19, 20]. The 2D flow exhibits large chaotic columns and whirls largely composed of pure fluid, and appears more stirred than mixed. The extent of the mixing regions are roughly comparable, with interpenetration of the 2D flow somewhat exceeding that of the 3D flow.

B. Growth

The growth of the mixing layer can be measured with integral quantities, such as product height H [14] or the mixing width W [10], or it can be measured with threshold values, which tend to be more sensitive to statistical variations. The integral product height is defined in terms of the horizontal mean of the mole fraction of the heavy fluid \bar{X} as

$$H = \int_{-\infty}^{\infty} X_P(\bar{X}) dz , \quad (2)$$

where the mole fraction and product mole fraction are given by

$$X = \frac{\rho - \rho_1}{\rho_2 - \rho_1}, \quad X_p(X) = \begin{cases} X/X_{st} & \text{for } X \leq X_{st} \\ (1 - X)/(1 - X_{st}) & \text{for } X > X_{st} \end{cases}, \quad (3)$$

typically using a stoichiometric mixture fraction $X_{st} = 1/2$. The integral mixing width [10] is given by

$$W = \int_{-\infty}^{\infty} \overline{X}(1 - \overline{X}) dz. \quad (4)$$

If the mixing region has a linear profile of \overline{X} across a height h , then $H = h/2$ and $W = h/6$. The integral product height H is shown in Fig. 3a; W gives the nearly same result at a factor of 2.9 lower. The ‘‘bubble’’ positions (h_b) and ‘‘spike’’ positions (h_s) relative to the position of the initial interface based on the 5% threshold values of mean concentration are shown in Fig. 3b; the total 5% threshold width is about $1.9H$. The mixing width for 2D and 3D runs (by all measures) begins the same. The mixing width for the 2Ds runs is nearly the same as for the 3D run at early times, while the mixing width for the 2Db runs is slightly narrower. The long-wavelength component in the 2Ds initial conditions may be responsible for more rapid initial growth of the mixing region compared with case 2Db. Up to $t = 15$, all of the mixing widths remain comparable. At later times, when the flows become better developed, the mixing width for the 2D runs exceeds that for 3D run by 30–40%. This trend is generally consistent with the results obtained by Youngs [10].

The growth rate (dH/dt) is shown in Fig. 4 for all 2D runs compared with the 3D run. Between $t = 10$ and 20, the 2D flows exhibit rapid growth at a time when the growth of the 3D mixing region slows at the onset of fully developed turbulence [14]. At later times the acceleration of the 2D flow appears to be comparable to the 3D flow; however this is when the 2D simulations are losing both large-scale horizontal resolution, which may affect the growth, and statistical sample.

C. Mixing

A global measure of mixedness based on product (Eqs. 2,3) is given by

$$\Xi = H^{-1} \int_{-\infty}^{\infty} \overline{X_p(X)} dz. \quad (5)$$

Another integral measure of mixedness [10] corresponding to Eq.(4) is given by

$$\Theta = W^{-1} \int_{-\infty}^{\infty} \overline{X(1-X)} dz, \quad (6)$$

which was found to be equivalent to Ξ [14]. Figure 5 shows that there are large differences in the level of mixedness between 2D and 3D simulations. After the initial entrainment at $t = 3$, the level of 3D mixedness continues to increase, reaching a plateau at $\Xi = 0.79$. On the other hand, the 2D mixedness, after a brief rise, declines to a level of $\Xi = 0.53$, independent of initial conditions. Youngs [10] cited values of $\Theta = 0.83$ for 3D versus 0.54 for 2D. This indicates that a substantial amount of pure fluid is being stirred, rather than mixed, in the 2D simulations.

D. Energy & Vorticity

The ratio of total resolved kinetic energy to released potential energy (KE/PE) is shown in Fig. 6a. At late times this ratio is about 0.5 in the 3D simulation while it grows to about 0.9 in the 2D simulations. This is consistent with the findings of Young et al. [6], who found $\text{KE/PE}(3\text{D}) = 0.42$ and $\text{KE/PE}(2\text{D}) > 0.8$ at late times in their DNS, and with Youngs [10], who found $\text{KE/PE}(3\text{D}) = 0.48$ and $\text{KE/PE}(2\text{D}) = 0.94$. There is thus a substantially greater conversion of potential energy to kinetic energy in 2D as opposed to 3D, with correspondingly less dissipation. The ratio of vertical kinetic energy to horizontal kinetic energy is shown in Fig. 6b. The 2D simulations on average have a noticeably higher ratio than the 3D simulation (about 0.7 versus 0.57 at late times), despite having one — rather than two — horizontal velocity components.

The total resolved kinetic energy and enstrophy per plane are shown in Fig. 7, where substantially more kinetic energy is observed at late times in the 2D simulations than in the 3D ones. On the other hand, there is much less large-scale, resolved enstrophy in the 2D simulations. The measure of enstrophy used here with variable density is $\Omega \equiv \boldsymbol{\omega}^2/2\rho$ (where $\boldsymbol{\omega}$ is the vorticity), which is governed by

$$\frac{\partial \Omega}{\partial t} + \nabla \cdot (\Omega \mathbf{u}) = \rho^{-1} [\boldsymbol{\omega} \boldsymbol{\omega} : \mathbf{S} + \boldsymbol{\omega} \cdot \mathbf{B} + \boldsymbol{\omega} \cdot (\nabla \times \rho^{-1} \nabla \cdot \boldsymbol{\sigma})] ; \quad (7)$$

$\mathbf{S} = (\nabla \mathbf{u} + \mathbf{u} \nabla)/2$ is the velocity strain tensor, $\mathbf{B} = \rho^{-2} \nabla \rho \times \nabla p$ is the baroclinic vector, and $\boldsymbol{\sigma}$ is the viscous stress tensor. The terms on the right-hand side of (7) are the production from

vortex stretching (which vanishes in 2D flow), production from baroclinicity, and viscous dissipation and redistribution, respectively. Vortex stretching in 3D turbulent flow is the mechanism that acts to transfer large-scale energy and enstrophy to small scales [18].

Note, however, that enstrophy is a small-scale quantity, the bulk of which resides in scales smaller than those resolved — at least in the 3D LES —, so the comparison using LES results may not be representative of all scales. To remedy this uncertainty, results from early times in a *fully resolved* direct numerical simulation (DNS) of RTI were examined, in which there was no dissipation or diffusion from SGS models, and a negligible amount from the numerical scheme. The DNS used the same numerical scheme, same 3:1 density ratio, similar small-scale, multimode initial conditions, and molecular viscosity and mass diffusivity with average Schmidt number of unity. A corresponding set of 10 2Db simulations were performed. These DNS results show the same trend in enstrophy as the large-scale LES data (Fig. 8). During the initial stages, baroclinicity is seen to be the dominant mechanism for generating enstrophy, but at late times in the 3D flow the vortex-stretching term becomes the dominant mechanism. Only the baroclinic production operates in the 2D flow, and a substantially lower amount of enstrophy is generated. Vertical profiles of horizontally averaged kinetic energy and enstrophy from the DNS are shown in Fig. 9 at a time $t = 12.3$ when $h(5\%) = 14.7$ in both 2D and 3D simulations; to facilitate comparison of the distributions, the 2D results have been scaled in the figures to same mean levels as the 3D results. It is seen that both kinetic energy and enstrophy in 2D have slightly narrower vertical extents with higher central peaks than in 3D; the 2D enstrophy is also skewed slightly more toward the heavy-density side of the domain. Very similar profiles are obtained for resolved kinetic energy and enstrophy in the LES results.

E. Midplane spectra and statistics

Horizontal power spectra of density and velocity fluctuations about their horizontally averaged means are computed in the plane (for 3D simulations) or on the line (for 2D simulations) at the position of the initial interface. For the 2D simulations, spectra are computed in one dimension and averaged over all realizations for the same time. For 3D simulations, spectra are computed in two dimensions (binned by absolute horizontal wavenumber k), or in one horizontal direction and averaged over the other horizontal direction. In all cases the

spectral function $E_\phi(k)$ for variable ϕ is related to the physical fluctuation “energy” by

$$\phi'^2/2 = \int_0^\infty E_\phi(k) dk , \quad (8)$$

where ϕ' is the rms value of ϕ about the horizontal average. The 2D spectra for the 3D simulations contain a small amount of power at high wavenumbers beyond the nominal (1D) filter cutoff due to contributions from both horizontal dimensions (i.e., from the “corner” regions in wavespace).

The spectra from the 2D and 3D simulations are shown in Fig. 10 at moderately late times when the flow structure is well developed. Because the 2D simulations develop large scales more rapidly than 3D ones, a time of $t = 22.5$ is compared with the spectra from the 3D simulations at $t = 30.0$ so that the peaks of the power spectra roughly coincide. Spectra are shown for the horizontal and vertical velocity components and the density. For all variables the 2D spectra are steeper than their 3D counterparts. The mid-wavenumber region in the spectrum for the vertical velocity component in the 3D simulation suggests a $k^{-5/3}$ dependence, while its 2D counterpart exhibits a steeper slope, closer to $k^{-5/2}$. The spectrum for horizontal velocity components from the 3D simulation does not have a discernable power-law region, but the spectra from the 2D simulations exhibits a region with $k^{-8/3}$ dependence. The 2D velocity spectra for RTI have slightly shallower slopes than for single-density homogeneous turbulence, where k^{-3} is predicted by theory and observed in decaying homogeneous 2D flow [2, 21]. The density spectrum shows an approximate $k^{-5/4}$ dependence in the 3D simulation and again a somewhat steeper $k^{-3/2}$ dependence in the 2D simulations. There is pronounced pileup of energy at low wavenumbers for the horizontal velocity components, as well as for density, in the 2D simulations, which is consistent with the larger ratios of horizontal to vertical kinetic energy seen in Fig. 6b.

The evolution of corresponding midplane integral lengths,

$$\lambda_\phi = \int_0^\infty k^{-1} E_\phi(k) dk / \int_0^\infty E_\phi(k) dk , \quad (9)$$

is shown in Fig. 11 for $\phi = u$ and w (values for ρ are close to those for w). The 2D integral lengths for w quickly become twice those for the 3D simulation, and the 2D values for u become 4 times greater than the 3D ones. At late times, λ_u for 2D runs is a substantial fraction of the horizontal numerical domain, which indicates that the 2D flow is becoming poorly resolved at large scales.

Probability density functions (PDFs) for the midplane mole fraction of the heavy fluid X are shown in Fig. 12; these PDFs are averaged over a range of late-time samples when the distributions are approximately stationary. The 3D distribution (averaged from $t = 21$ to 35) has a “convex” structure with a peak at $X = 0.40$ and only small amounts of pure fluid ($X = 0, 1$) present. The 2D distribution (averaged from $t = 15$ to 25) is quite different, showing a “concave” structure with large amounts of pure fluid, more reminiscent of the outer, poorly mixed regions of the 3D flow near the spike and bubble fronts. The PDF distribution in height is shown in Fig. 13 for 3D (at $t = 30.0$) and 2D (at $t = 22.5$) simulations. For 3D simulations, the peak of the distribution marches from light to heavy as one ascends through the mixing region; there is a broad, well-mixed region around the midplane with width comparable to H . There is no such region evident in the poorly mixed 2D simulation results.

The history of rms values for midplane density and vertical velocity fluctuations, and their correlation to one another, are shown in Fig. 14. The 2D rms values exceed their 3D counterparts considerably at late times when ρ' and w'/Agt appear to reach asymptotes. However, the correlation between density and vertical velocity fluctuations is considerably lower in the 2D flows than in the 3D case, which is symptomatic of a greater amount of entrained pure fluid in the 2D case. Also, unlike the 3D case, the 2D correlation between ρ and w continues to drop and does not reach an asymptotic value. Note that the ratio $w'/2Agt$ is defined by Ramaprabhu & Andrews [22] as a measure of the acceleration coefficient α for quadratic growth. In the 3D simulation this ratio asymptotes at late times to a value of 0.033, while the 2D simulations produce 0.055. A better overall collapse of the simulation data is obtained in Fig. 14b using the effective Atwood number $A_e = \rho'/\bar{\rho}$ instead of A to scale w' ; late-time values of $w'/2A_e gt$ are about 0.068 for the 3D case and 0.076 for the 2D case. These results are consistent with the idea that reduced effective Atwood number in 3D miscible flow is associated with slower growth of the mixing region [14, 23]. Note that the reduction in A_e in the LES is a result of mass diffusion by the SGS model and can be considered “physical” to the extent the model is representative of turbulence processes affecting the resolved scales.

IV. CONCLUSIONS

Using two-dimensional and three-dimensional large-eddy simulations of Rayleigh-Taylor instability with similar initial conditions, we find that the 2D cases produce roughly comparable growth rates to 3D cases in the early stages of nonlinear growth, but at late times the 3D flow becomes fully turbulent and its growth becomes substantially slower than the 2D case. This is consistent with previous observations by Youngs [10]. The 2D flow, unlike the 3D flow, does not become well mixed at late times, as made evident by flow field structure, PDFs, and direct measures of mixedness.

The 2D RTI flow develops larger structures more rapidly than the 3D flow, especially in the horizontal velocity component, and a much larger fraction of released potential energy winds up in kinetic energy. This is consistent with the standard picture that in 3D RTI there is energy transfer both to large scales due to mode coupling and to small scales due to the turbulent energy cascade, while in 2D flow experiences vortex pairing and energy transfer that is preferentially toward large scales.

While 2D simulations of fully 3D RTI flows may provide a rough estimate of growth rates at early times, they do not produce accurate late-time turbulent growth rates and mixing statistics, and they are clearly no substitute for full 3D simulations. While attempts to re-tune subgrid-scale models to account in a crude way for lower dimensionality have had modest success in improving predictions for some statistics in convective flows, it is recognized that the resulting 2D pseudo-structures are not physical representations of real 3D flow [3]. Nor is it clear at this point if such an approach is viable for RTI applications. Finally, models of RTI growth that attempt to distinguish between 2D and 3D growth *at late time* need to take account of the very different physical mechanisms that operate in each case.

Acknowledgments

The author thanks Drs. P.L. Miller and A.W. Cook for their valuable observations and advice, and the referees for recommendations that improved the quality of this paper. This work was performed under the auspices of the U.S. Department of Energy by the University of California Lawrence Livermore National Laboratory under contract No. W-7405-Eng-48.

-
- [1] J. T. Waddell, C. E. Niederhaus, and J. W. Jacobs, “Experimental study of Rayleigh-Taylor instability: Low Atwood number liquid systems with single-mode initial perturbations,” *Phys. Fluids* **13**, 1263 (2001).
- [2] R. H. Kraichnan and D. Montgomery, “Two-dimensional turbulence,” *Rep. Prog. Phys.* **43**, 547 (1980).
- [3] C.-H. Moeng, J. C. McWilliams, R. Rotunno, P. P. Sullivan, and J. Weil, “Investigating 2D modeling of atmospheric convection in the PBL,” *J. Atm. Sci.* **61**, 889 (2004).
- [4] N. N. Anuchina, V. I. Volkov, V. A. Gordeychuk, N. S. Es’kov, O. S. Ilyutina, and O. M. Kozyrev, “Numerical simulations of Rayleigh-Taylor and Richtmyer-Meshkov instability using mah-3 code,” *J. Comput. Appl. Math.* **168**, 11 (2004).
- [5] J. Kane, D. Arnett, B. A. Remington, S. G. Glendinning, G. Bazán, et al., “Two-dimensional versus three-dimensional supernova hydrodynamic instability growth,” *Astrophys. J.* **528**, 989 (2000).
- [6] Y.-N. Young, H. Tufo, A. Dubey, and R. Rosner, “On the miscible Rayleigh-Taylor instability: two and three dimensions,” *J. Fluid Mech.* **447**, 377 (2001).
- [7] S. V. Weber, G. Dimonte, and M. M. Marinak, “Arbitrary Lagrange-Eulerian code simulations of turbulent Rayleigh-Taylor instability in two and three dimensions,” *Laser and Particle Beams* **21**, 455 (2003).
- [8] G. Dimonte, D. Youngs, A. Dimits, S. Weber, M. Marinak, et al., “A comparative study of the Rayleigh-Taylor instability using high-resolution three-dimensional numerical simulations: the Alpha group collaboration,” *Phys. Fluids* **16**, 1668 (2004).
- [9] D. L. Youngs, “Three-dimensional numerical simulation of turbulent mixing of Rayleigh-Taylor instability,” *Phys. Fluids A* **3**, 1312 (1991).
- [10] D. L. Youngs, “Numerical simulations of mixing by Rayleigh-Taylor and Richtmyer-Meshkov instabilities,” *Laser and Particle Beams* **12**, 725 (1994).
- [11] V. N. Goncharov, “Analytical model of nonlinear, single-mode, classical Rayleigh-Taylor instability at arbitrary Atwood numbers,” *Phys. Rev. Letters* **88**, 134502 (2002).
- [12] D. Oron, L. Arazi, D. Kartoon, A. Rikanati, U. Alon, and D. Shvarts, “Dimensionality dependence of the Rayleigh-Taylor and Richtmyer-Meshkov instability late-time scaling laws,”

- Phys. Plasmas **8**, 2883 (2001).
- [13] D. Shvarts, D. Oron, D. Kartoon, A. Rikanati, O. Sadot, et al., “Scaling laws of nonlinear Rayleigh-Taylor and Richtmyer-Meshkov instabilities in two and three dimensions,” *C. R. Acad. Sci. Paris* **IV**, 719 (2000).
- [14] A. W. Cook, W. Cabot, and P. L. Miller, “The mixing transition in Rayleigh-Taylor instability,” *J. Fluid Mech.* **511**, 333 (2004).
- [15] S. K. Lele, “Compact finite difference schemes with spectral-like resolution,” *J. Comp. Phys.* **103**, 16 (1992).
- [16] P. E. Dimotakis, “The mixing transition in turbulence,” *J. Fluid Mech.* **409**, 69 (2000).
- [17] T. T. Clark, “A numerical study of the statistics of a two-dimensional Rayleigh-Taylor mixing layer,” *Phys. Fluids* **15**, 2413 (2003).
- [18] H. Tennekes and J. L. Lumley, *A First Course in Turbulence* (The MIT Press, 1972).
- [19] W. H. Cabot, A. W. Cook, P. L. Miller, D. E. Laney, M. C. Miller, and H. R. Childs, “Large-eddy simulation of Rayleigh-Taylor instability,” *Phys. Fluids* **17**, 091106 (2005).
- [20] P. L. Miller, W. H. Cabot, and A. W. Cook, “Which way is up? A fluid dynamics riddle,” *Phys. Fluids* **17**, 091110 (2005).
- [21] A. Bracco, J. C. McWilliams, G. Murante, A. Provenzale, and J. B. Weiss, “Revisiting freely decaying two-dimensional turbulence at millennial resolution,” *Phys. Fluids* **12**, 2931 (2000).
- [22] P. Ramaprabhu and M. J. Andrews, “Experimental investigation of Rayleigh-Taylor mixing at small Atwood numbers,” *J. Fluid Mech.* **502**, 233 (2004).
- [23] E. George and J. Glimm, “Self-similarity of Rayleigh-Taylor mixing rates,” *Phys. Fluids* **17**, 054101 (2005).

V. FIGURE CAPTIONS

FIG. 1: Midplane horizontal power spectra of density at $t = 0$ for the 3D and 2Db simulations (thick line) and the 2Ds simulations (thin line). The 3D and 2Db spectra are identical by design.

FIG. 2: Vertical slice of density from the 3D simulation (top) compared with the density field from a 2D simulation (bottom), both at $t = 25$. Black is heavy fluid, and white is light fluid.

FIG. 3: (a) Integral product height and (b) 5% threshold values of mean density for the 3D (solid lines), 2Db (dashed lines) and 2Ds (dot-dashed lines) simulations. The standard deviation in the 2D runs is about 7% in (a) and 10% in (b) at late times.

FIG. 4: Growth rate of the integral product width for 3D (solid line) and 2D (dashed line) simulations. The dotted line is a linear fit to the 3D data at late times, giving an acceleration coefficient $\alpha_H \approx 0.025$, corresponding to $\alpha \approx 0.027$ for bubble growth based on a 1% threshold [14].

FIG. 5: Mixedness measure Ξ for 3D (solid line), 2Db (dashed line), and 2Ds (dot-dashed line) simulations. The standard deviation is about 7% at late times for the 2D runs. Values for Θ are nearly identical.

FIG. 6: (a) The ratio of total resolved kinetic energy to released potential energy and (b) the ratio of total resolved horizontal to vertical kinetic energy for the 3D (solid line), 2Db (dashed line) and 2Ds (dot-dashed line) simulations. The standard deviation at late times in the 2D runs is about 1% in (a) and 15% in (b).

FIG. 7: Total resolved (a) kinetic energy and (b) enstrophy from 3D LES (solid lines) and 2D LES (dashed lines), normalized per plane.

FIG. 8: (a) Global enstrophy and (b) global enstrophy production rates from vortex stretching and baroclinicity from 3D DNS (solid lines) and 2D DNS (dashed lines), normalized per plane.

FIG. 9: Vertical profiles of horizontally averaged (a) kinetic energy and (b) enstrophy from 3D DNS (solid lines) and 2D DNS (dashed lines) at $t = 12.3$ and $h(5\%) = 14.7$; the 2D kinetic energy was scaled by a factor of 0.502 and the 2D enstrophy by 2.71.

FIG. 10: Midplane horizontal power spectra of (a) vertical velocity component, (b) horizontal velocity components, and (c) density for the 3D simulations at $t = 30.0$ (solid lines), and for the average of all 2D simulations at $t = 22.5$ (dashed lines). Reference slopes are indicated by the short fiducial lines.

FIG. 11: Midplane horizontal integral lengths of horizontal velocity components (u , dashes) and vertical velocity component (w , solid) for the 3D and 2D simulations. The horizontal domain size is $L = 144$ for comparison.

FIG. 12: Probability density functions of the midplane mole fraction of the heavy fluid for the 3D (solid line) and 2D (dashed line) simulations.

FIG. 13: (Color online) Probability density functions of the mole fraction of the heavy fluid X versus height for (a) 3D simulations at $t = 30.0$ and (b) 2D simulations at $t = 22.5$.

FIG. 14: Midplane density and vertical velocity fluctuations for the 3D (solid lines) and 2D (dashed lines) simulations. In (a) the correlation coefficient for density and vertical velocity fluctuations $C(\rho, w)$ is also shown.

Figures

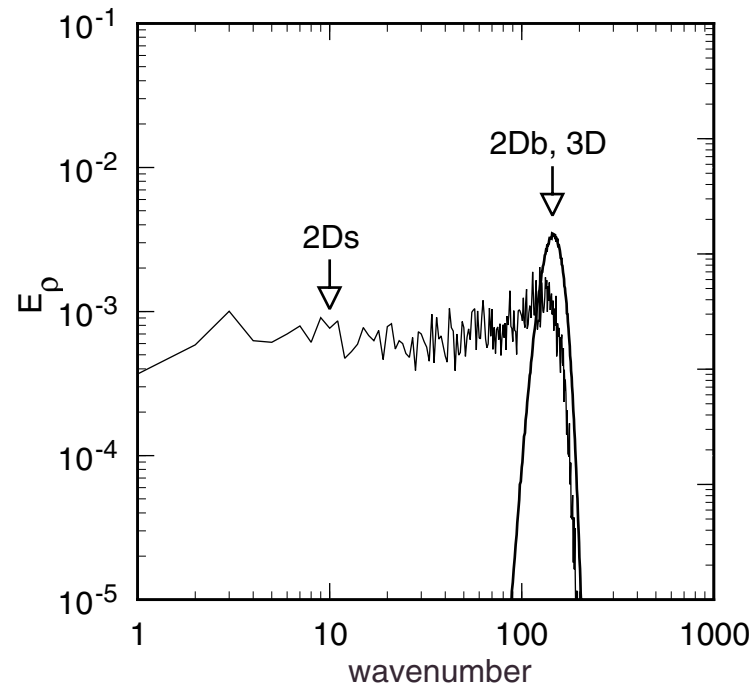


FIG. 1: Cabot, Physics of Fluids

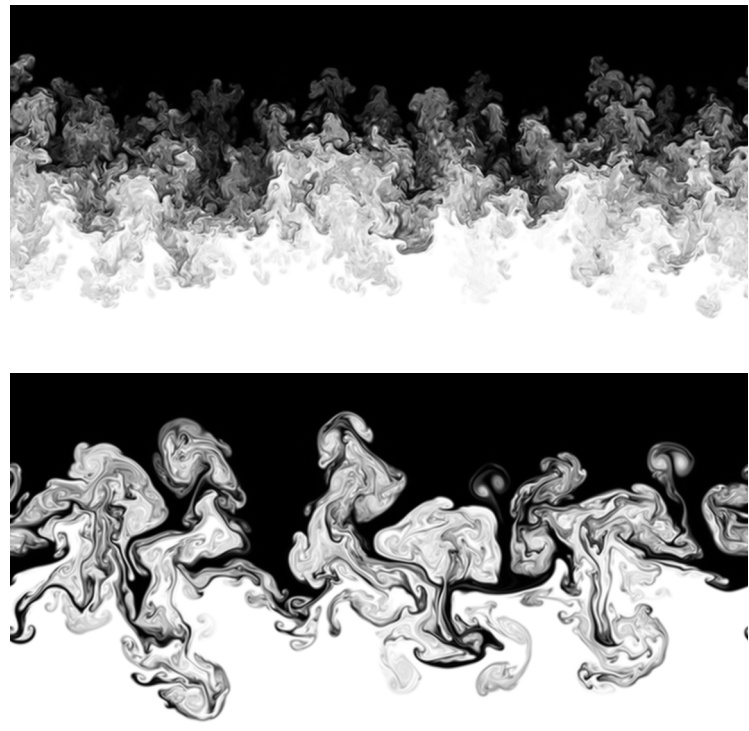


FIG. 2: Cabot, Physics of Fluids

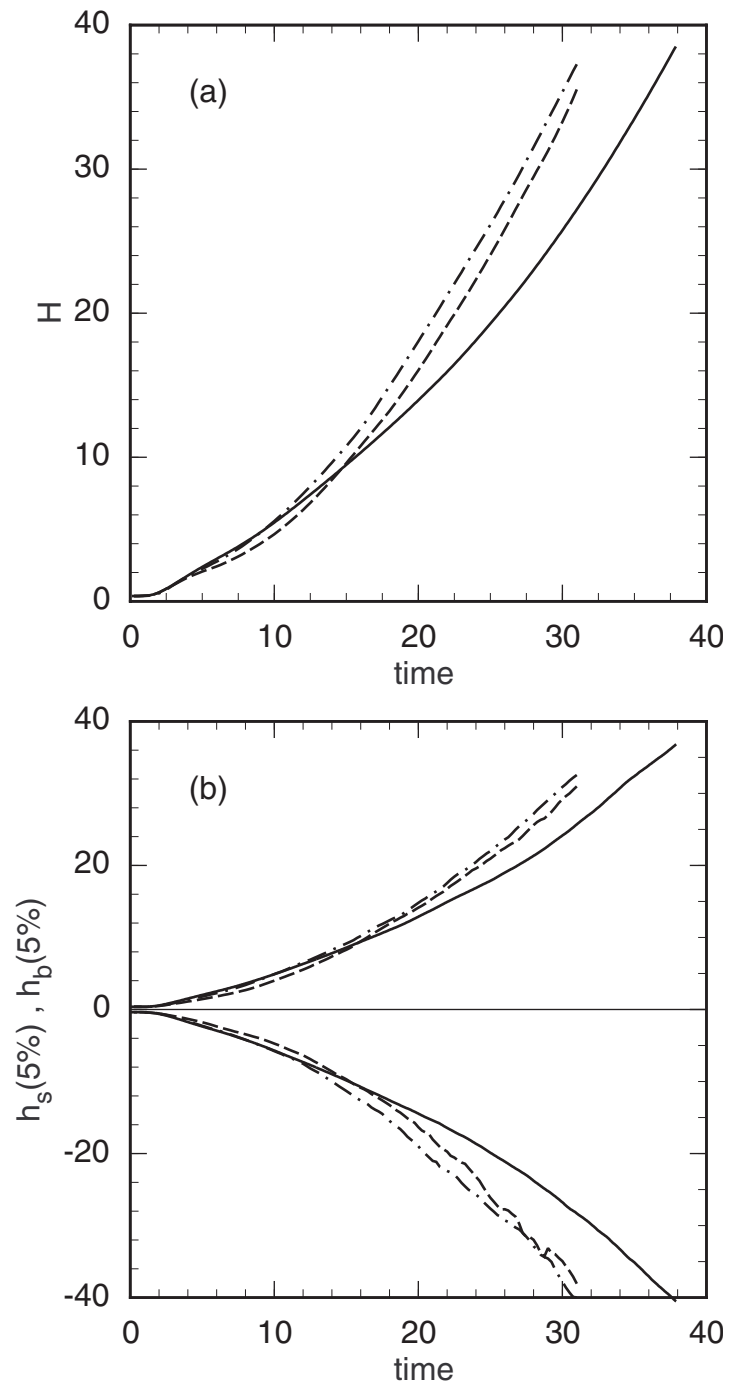


FIG. 3: Cabot, Physics of Fluids

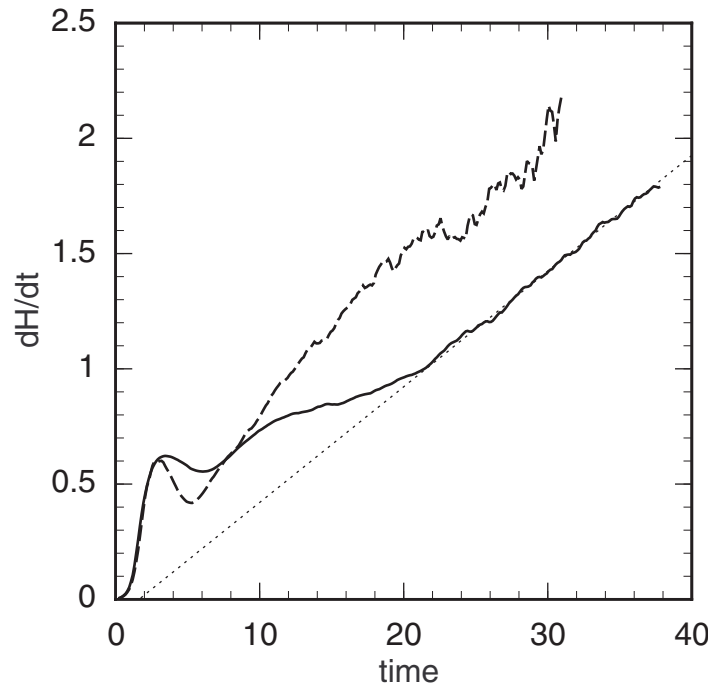


FIG. 4: Cabot, Physics of Fluids

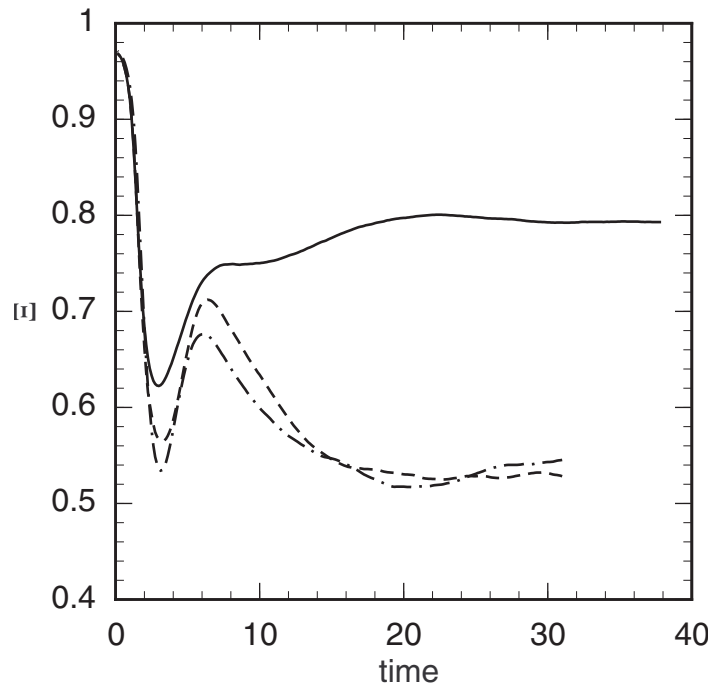


FIG. 5: Cabot, Physics of Fluids

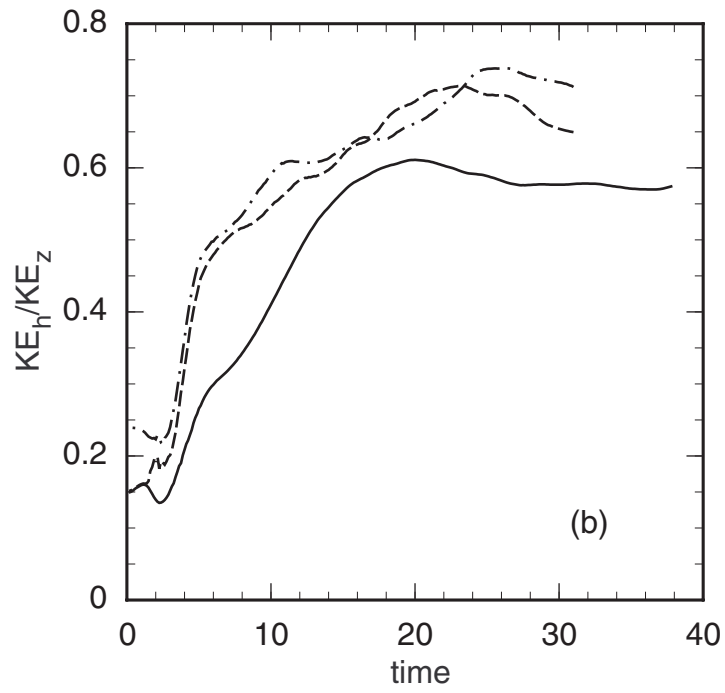
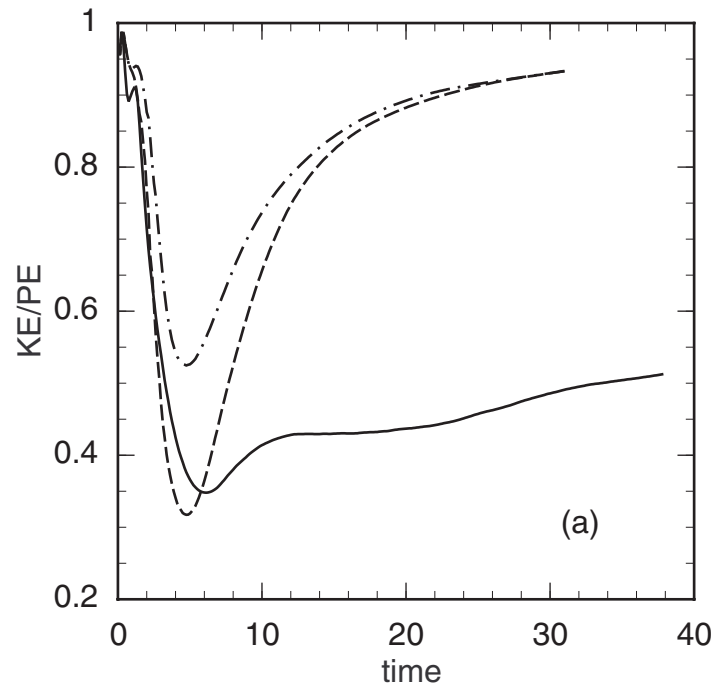


FIG. 6: Cabot, Physics of Fluids

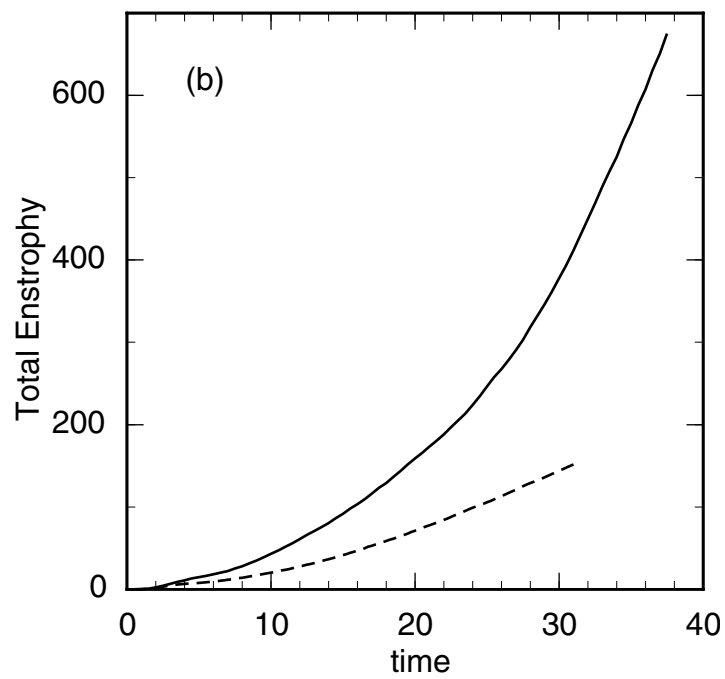
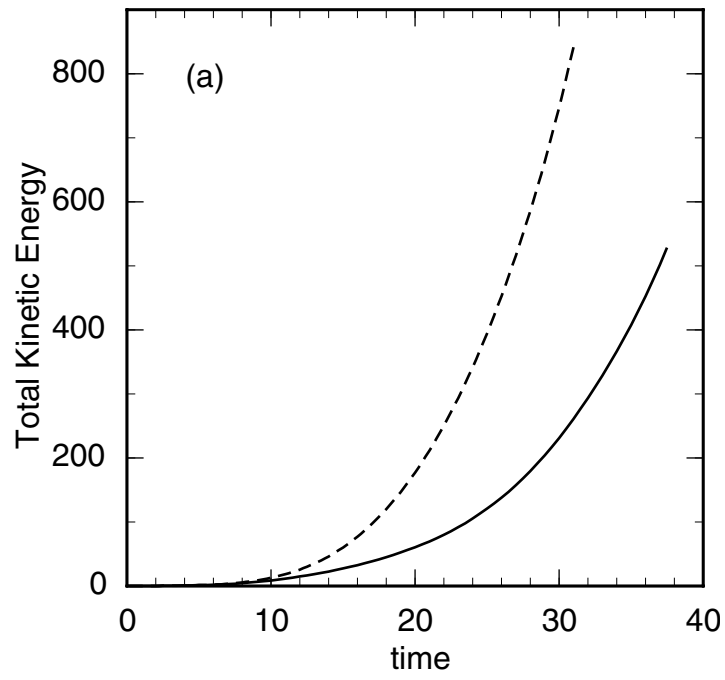


FIG. 7: Cabot, Physics of Fluids

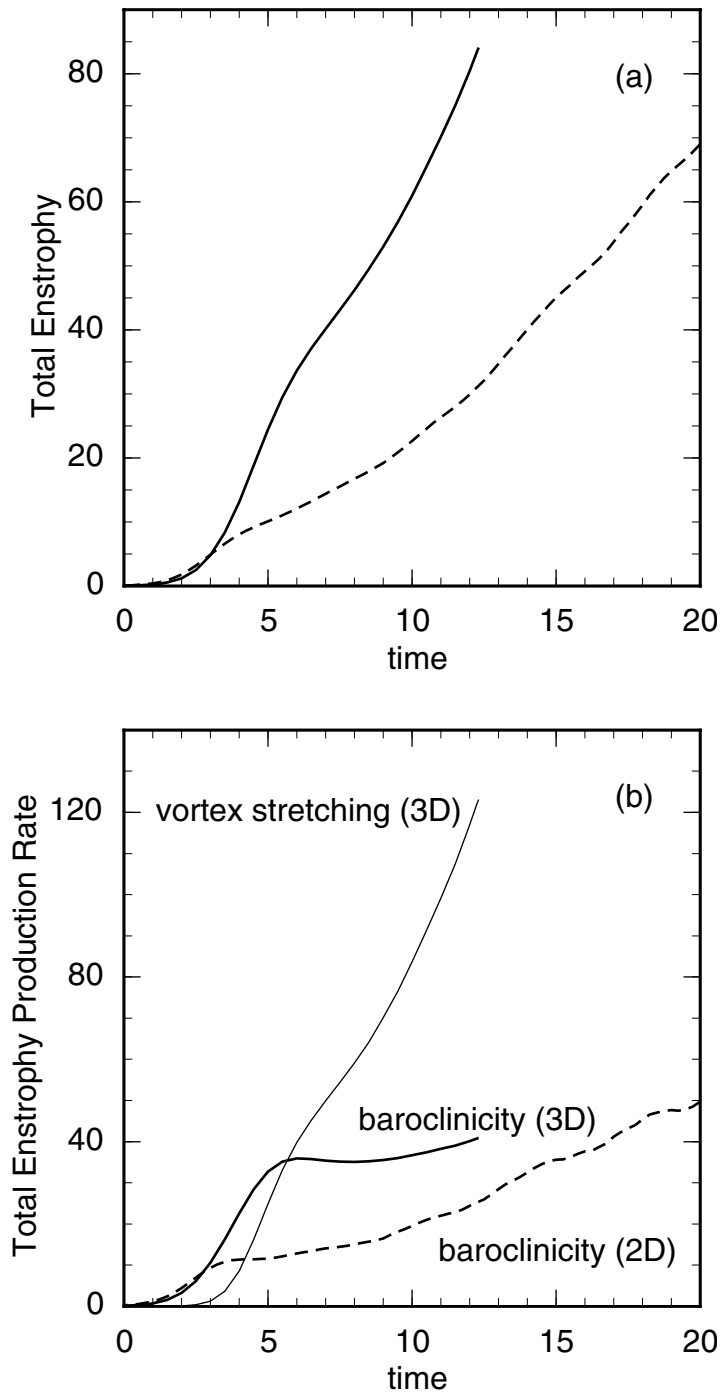


FIG. 8: Cabot, Physics of Fluids

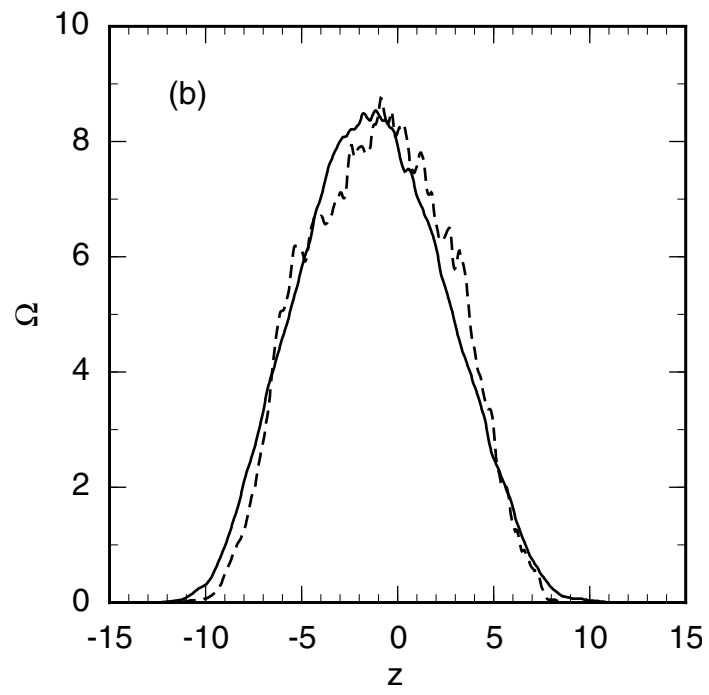
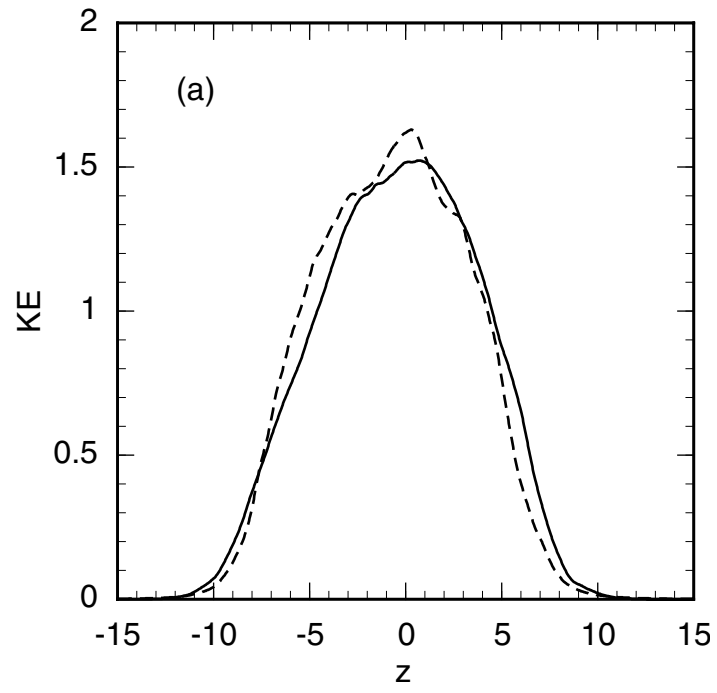


FIG. 9: Cabot, Physics of Fluids

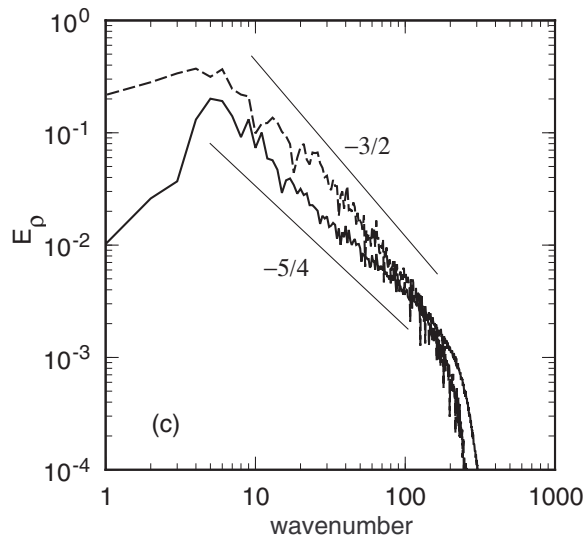
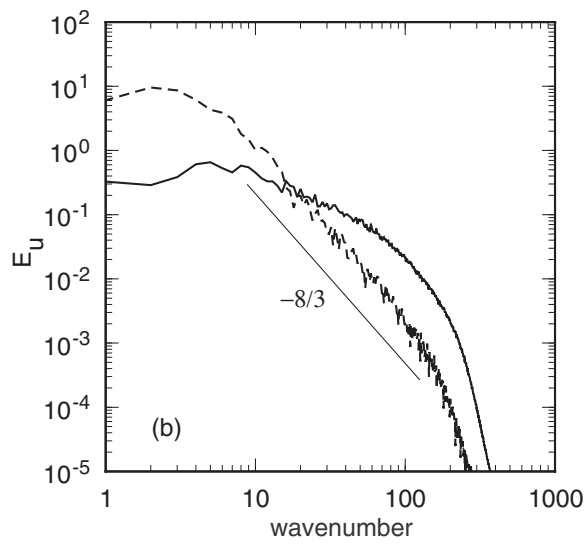
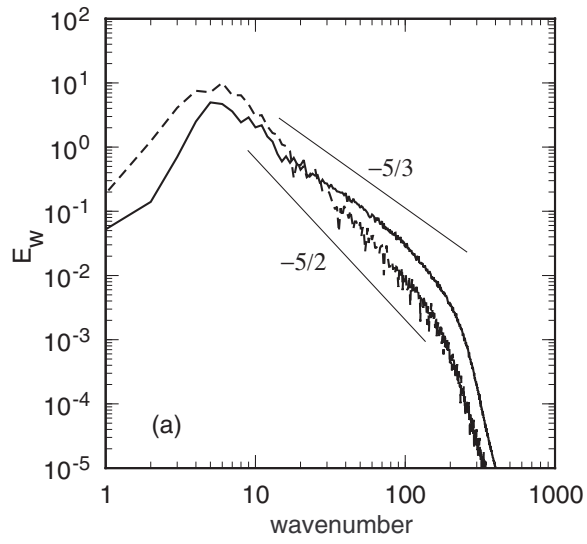


FIG. 10: Cabot, Physics of Fluids

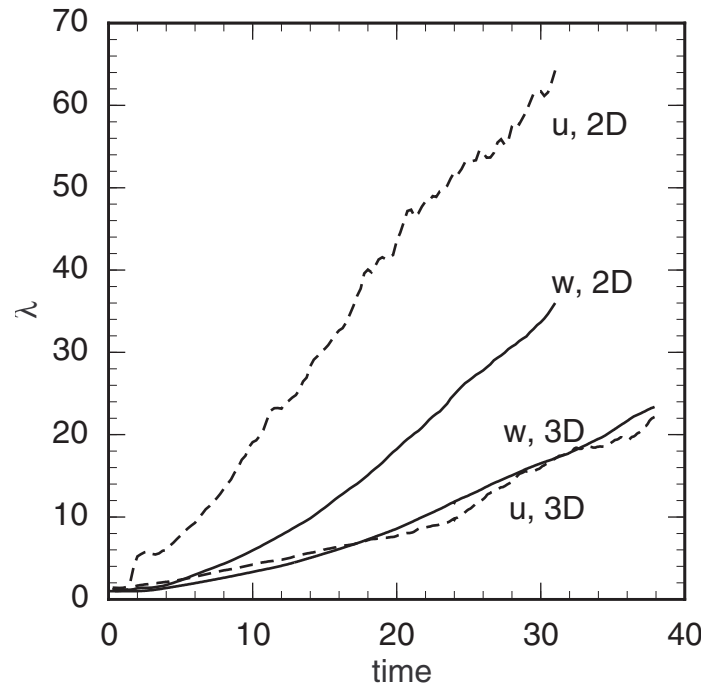


FIG. 11: Cabot, Physics of Fluids

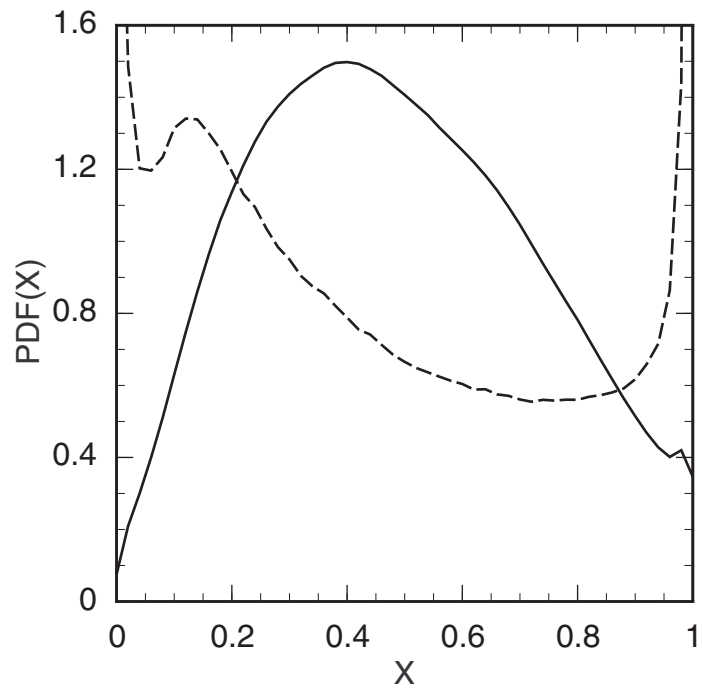


FIG. 12: Cabot, Physics of Fluids

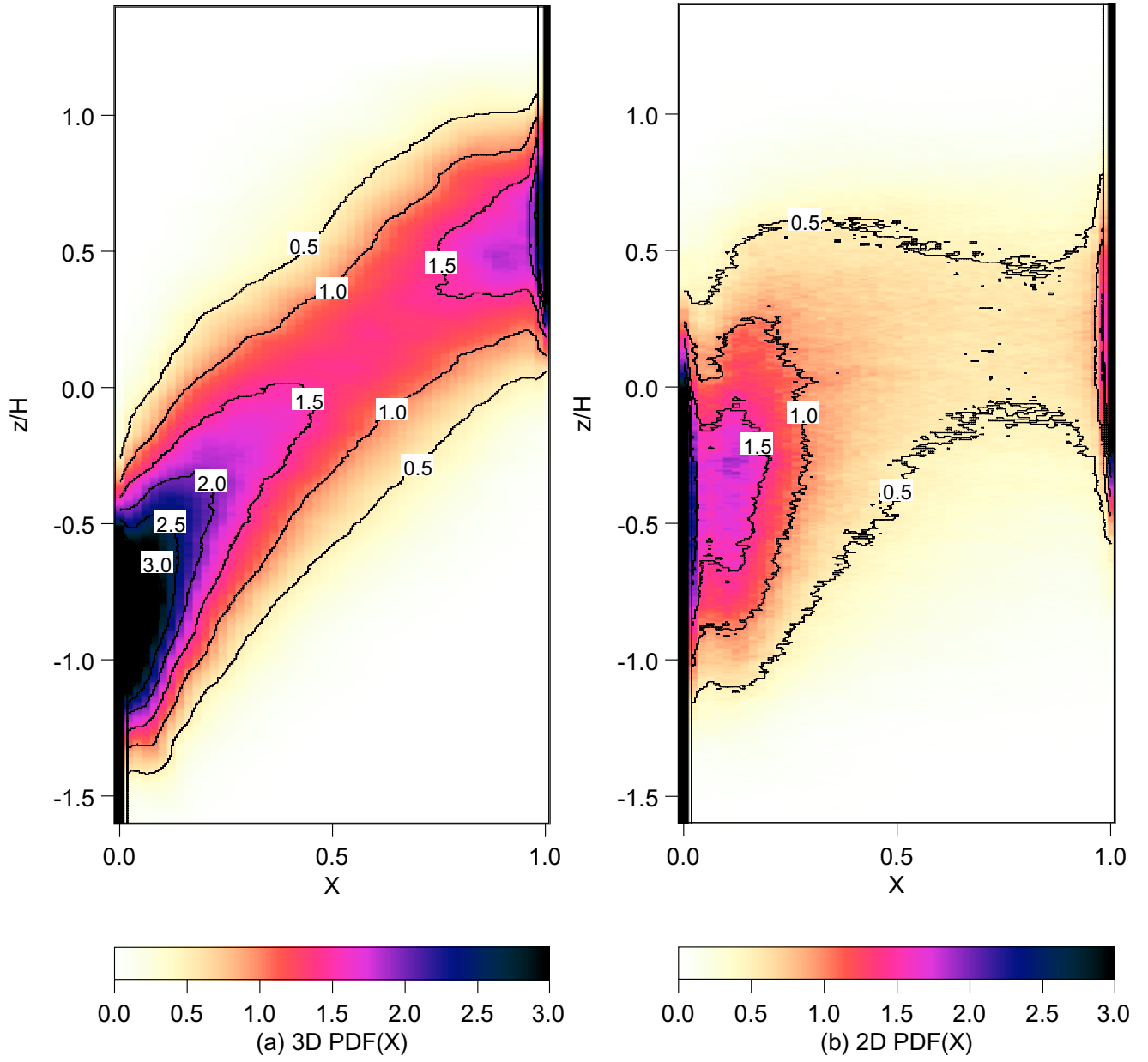


FIG. 13: Cabot, Physics of Fluids

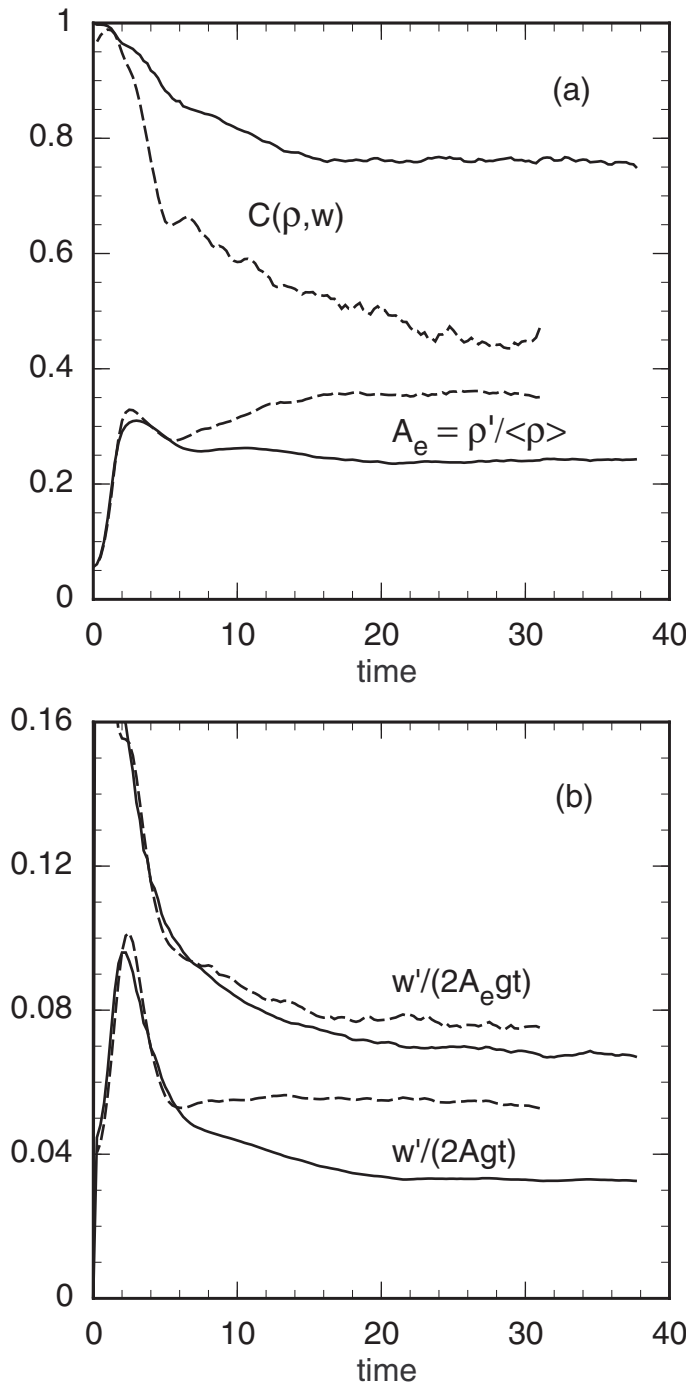


FIG. 14: Cabot, Physics of Fluids